A Low-Toxic Colloidal Quantum Dots Sensitized IGZO Phototransistor Array for Neuromorphic Vision Sensors

Tong Chen[1], Shijie Zhan[2], Benxuan Li[2,3], Bo Hou[2], Hang Zhou[1]**

1 School of Electronic and Computer Engineering, Peking University Shenzhen Graduate School, Shenzhen, 518055, China;

2 School of Physics and Astronomy, Cardiff University, The Parade, Cardiff, CF24 3AA, UK;

3 International Collaborative Laboratory of 2D Materials for Optoelectronics Science and Technology of Ministry of Education, Institute of Microscale Optoelectronics, Shenzhen University, Shenzhen 518060, China

E-mail: houb6@cardiff.ac.uk, zhouh81@pkusz.edu.cn

Keywords: phototransistors, IGZO, quantum dots, neuromorphic sensor

The rapid development of optoelectronic devices with biomimetic synaptic behaviour holds significant potential for neuromorphic visual applications. However, considerable challenges remain including convenient device fabrication and low toxicity materials innovation. Here, a heterojunction phototransistor is constructed using low-toxic CuZnInSSe colloidal quantum dots and amorphous IGZO, which demonstrates high specific detectivity of 3.4×10^{15} Jones in visible light spectrum. Moreover, it is found that the photoresponse speed can be controlled via a ligand exchange treatment, through which the response speed can be adjusted from 0.3 s to 11 s. This enables the device operate in two distinct modes: a typical fast sensing mode and a neuromorphic visual mode. In the neuromorphic visual mode, the device's synaptic behaviour can be tuned by manipulating light pulse intensity, frequency, wavelength, and gate voltage. As a demonstration, a phototransistor array effectively implements image pre-processing functions, including colour recognition, visual memorizing, and forgetting.

1. Introduction

Nowadays, Moore's law is inexorably approaching the limits of integrated circuit technology, while the explosive growth of the Internet of Things has led to an unprecedented increase of data. In this context, traditional computing systems built on von Neumann architecture chips find themselves ill-equipped to cope with the escalating computational demands of the big data era. Consequently, there is an urgent need for a new computing paradigm and advanced data processing terminals. Notably, vision sensing stands as a typical

data-intensive application and represents a pivotal research avenue in the contemporary technological landscape.[1]

Artificial neuromorphic vision systems currently rely on arrays of image sensors to convert optical signals into electrical data, which is subsequently forwarded to neuromorphic chips for further processing. This conventional approach results in a substantial production of redundant data, contributing to elevated power consumption and signal delay.[2] In contrast, sensory neurons within the human retina not only detect light stimuli but also undertake preliminary image processing tasks in a highly energy-efficient manner. This intrinsic capability occurs before the more intricate stages of visual signal processing within the human visual cortex. Consequently, the quest to develop multifunctional electronic devices capable of integrating sensing, storage, and processing functions has emerged as a pivotal challenge in the realm of efficient artificial vision network systems. Recent years have witnessed the emergence of novel semiconductor devices designed to emulate synaptic behaviours in the context of neuromorphic vision sensors. [1,3] These devices encompass a range of technologies, including photo-resistive memory, nano-memristors, and phototransistor devices.[3–11] Leveraging distinct optical response characteristics, such as linear or nonlinear responses, they facilitate image feature enhancement and image recognition within sensor arrays. In the realm of image information preprocessing, Chai's research team has devised a two-end structured synaptic device capable of sensing ultraviolet light while offering adjustable synaptic properties through varying illumination duration and intensity. Utilizing such a photo-resistive memory array image sensor in conjunction with artificial neural networks, it is possible to construct a neuromorphic vision system that emulates the human retina's functions.[4] This innovative approach streamlined the circuitry of neuromorphic vision systems and reduces power consumption, thereby enhancing the processing efficiency of dynamic visual information. Additionally, Hu and fellow researchers have introduced a controlled ultraviolet-ultrasensitive neuromorphic visual sensor. This sensor leveraged organic phototransistors as functional units to integrate sensing, memory, and processing capabilities. By harnessing wavelength-selective responses and multilevel optical memory features, they've crafted an artificial neural network capable of extracting and identifying previously imperceptible ultraviolet rays.[6] Presently, by emulating the characteristics and operating principles of these emerging devices, substantial progress has been made in achieving efficient and rapid neuromorphic visual sensing capabilities.

However, a substantial portion of these endeavours relies on devices founded on novel semiconductor materials like nanowires and two-dimensional layered material semiconductors. This reliance on novel materials presents a few challenges. First, the preparation and processing

technologies for these materials remain in a nascent state, hindering their large-scale production and elevating manufacturing costs, thereby impeding their swift advancement. Second, the performance uniformity and stability of devices constructed from these new nanomaterials frequently require enhancements, creating a bottleneck in the systematic development of complex, multifunctional neuromorphic vision sensors. Moreover, it's important to note that some of these materials contain heavy metal elements, such as lead and cadmium, posing potential environmental and health hazards.

The metal-oxide transistor boasts several key advantages, including low off-state current, high mobility, minimal subthreshold swing, and excellent uniformity over large areas.[12–14] In its role as a phototransistor, it offers adjustable photoelectric detection performance and seamlessly integrates with various photoelectric materials.[15–18] Its adaptability allows for the emulation of neural synapse behaviours and function through the application of electrical and optical signals, making metal-oxide phototransistors and their arrays well-suited as research platforms for neuromorphic vision network simulation systems.[19–22] In addition, quantum dots derived from Group I-III-VI, Group II-VI, and similar constituents have emerged as the predominant light-absorbing materials in nanoparticle technology. These quantum dots offer the advantage of tuneable band gap widths based on size and composition, while exhibiting strong light absorbance. [23–26] Significantly, they are devoid of toxic heavy metal elements, rendering them environmentally friendly. Among these materials, a kind of copper chalcogenide colloidal quantum dots (CuInZnSSe, CIZS QDs) stand out as a particularly well-suited candidate for the light-absorbing layer of phototransistors. Their characteristics, such as ease of large-scale preparation and low toxicity, make them highly compatible with the development of neuromorphic bioinspired systems.

In this report, a combination of the low-toxic CIZS QDs and In-Ga-Zn-O thin-film transistor (IGZO TFT) is utilized to fabricate heterojunction phototransistors. When subjected to 520 nm illumination with a power of 0.1 μW, the heterojunction phototransistor based on CIZS QDs and IGZO achieved a high responsivity (R) of 60 AW^{-1} and a specific detectivity (D*) of 2×10^{15} Jones, respectively, with gate voltage (V_G) of -0.9 V and drain voltage (V_D) of 1 V. Surface ligand treatment was further employed to modulate the response speed, enabling the demonstration of a neuromorphic visual memory image sensor. To further enhance the versatility of the device, we have regulated its response time through surface ligand treatment. Devices treated with short-chain ligands exhibit a response time of approximately 0.3 s. In contrast, unprocessed quantum dot materials, characterized by long-chain ligands, exhibit slower response times but display tuneable photosynaptic behaviours. The array formed by

these devices demonstrates functions such as memory, image enhancement, and image forgetting. Such multifaceted capabilities position this device as having significant potential for application in the field of bionic vision signal preprocessing.

2. Result and discussion

The schematic depiction of the CIZS QDs/IGZO heterojunction phototransistor is illustrated in **Figure 1**a. This device comprised a layer of QDs atop the channel layer of the IGZO TFT, adopting a bottom-gate top-contact configuration. The specific fabrication process is elucidated in the experimental methods section. Figure S1a is an optical microscope image of the device with a width-to-length ratio (W/L) of 100/100μm. Figure 1b presents a cross-sectional scanning electron microscope (SEM) image of the heterojunction region, revealing respective thicknesses of approximately 180 nm for the insulation layer, 36 nm for IGZO, and 102 nm for CIZS QDs. Supplementary Figure S1b displays a planar SEM image of the CIZS QDs thin film overlaid on the IGZO layer. It is discernible that the surface exhibited a smooth and uniform morphology. The absorption spectrum of the CIZS QDs thin film is depicted in Figure 1c, demonstrating pronounced absorption within the 400-650 nm range. A high-resolution transmission electron microscope (TEM) image in the inset provides insight into the uniformity of the QDs, each exhibiting a diameter ranging between 2-3 nm. The determination of the band location of CIZS QDs was derived from the ultraviolet photoelectron spectroscopy (UPS) (Figure S2) and the Tauc diagram corresponding to the absorption spectrum (Figure S3). As for IGZO, its energy band characteristics was drawn from data in our previous research.[15] The heterojunction band alignment of CIZS QDs/IGZO is showcased in Figure 1d. When QDs absorb photons, electron-hole pairs were generated. Electrons readily ingress the IGZO layer, generating photocurrent due to the commendable electron mobility of IGZO absorbed by the electrode. Simultaneously, photogenerated holes persist within the QDs layer, augmenting the photocurrent of the device. This phenomenon also led to a notable negative drift in the threshold voltage. Figure S4 displays the transfer characteristic curves of various IGZO TFTs within the same batch and shows a relatively high electrical performance uniformity of the device. Table S1 in the supplementary information outlines the average values of key performance parameters for the five transistor devices, revealing low off-state current, small subthreshold swing, and relatively high on/off ratio. The electron mobility in the IGZO TFT falls within the typical range, underscoring the overall commendable performance of the device. Figure S5 shows the response of the phototransistor under three distinct wavelengths of light (480 nm, 520 nm, and 630 nm) subsequent to the introduction of CIZS QDs. Evidently, the device manifested an

obvious optical response to all three types of light, rendering it apt for light detection applications.

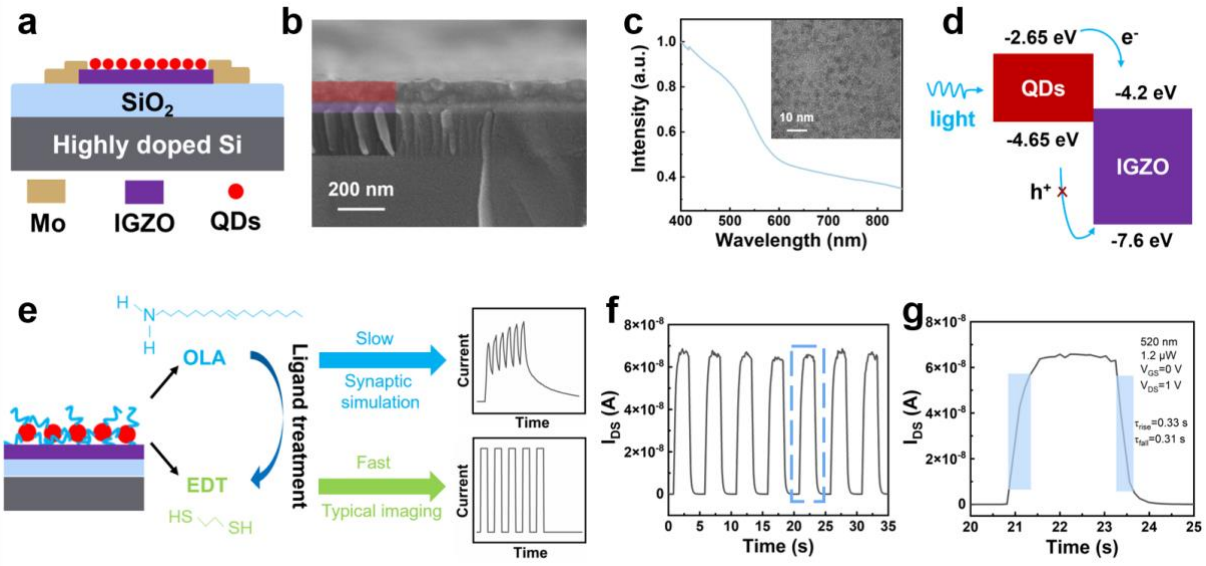

Figure 1. (a) Device structure diagram of the CIZS QDs/IGZO heterojunction phototransistor. (b) SEM image of the cross-section of the device. The red, purple and black blocks represent CIZS QDs, IGZO and SiO_2 layers, respectively. (c) The absorption spectrum and high-resolution TEM image of CIZS QDs. (d) Energy band diagram of CIZS QDs/IGZO heterojunction. (e) Ligand exchange treatment and corresponding application. (f) The transient photocurrent response of the phototransistor after ligand treatment. (g) Magnification of a cycle in (f).

CIZS QDs were synthesized through a hot injection process employing oleylamine (OLA), a kind of long-chain alkane molecules. The synthesis method of QDs is descripted in experimental part. OLA served the critical function of maintaining colloidal stability in a non-polar solvent, thus preventing the agglomeration of QDs. [23] However, it is important to note that OLA, while effective as a stabilizing agent, is non-conductive. This non-conductivity impeded charge transfer within the QDs, significantly hampering the response speed of phototransistors. [24] In addressing this limitation, we have implemented a solid-phase surface ligand exchange treatment to replace the long-chain ligands on the QDs with short-chain ligands. Figure 1e provides a visual representation of how this ligand exchange process impacted the response speed of the phototransistor, rendering the device adaptable for various application scenarios. Phototransistors employing long-chain ligand QDs exhibit sluggish response times characteristic of optical synapses, which find relevance in bionic vision applications. Subsequent to ligand exchange, device response times are markedly improved, making them

more suitable for conventional imaging applications. The short-chain ligand used in our study is the 1,2-Ethanedithiol (EDT), which has been effectively employed in numerous applications involving lead sulfide QDs. [27–29] This molecule enhanced charge transfer within QD materials, reducing carrier recombination and ultimately diminishing response times. Following ligand treatment, the time response curve of the QD device is presented in Figure 1f, with Figure 1g showing the curve for a single cycle. The device demonstrated a rise time of 0.33 s and a fall time of 0.31 s. This faster response speed in amorphous oxide phototransistors aligned with the requirements of standard image sensing applications. Figure S6 illustrates the device response following ligand treatment under 520 nm illumination, revealing minimal deviation from the untreated device's response. Consequently, this treatment methodology exerted virtually no adverse impact on the device's optical response performance, while notably enhancing its response speed.

The response speed of the phototransistor without ligand exchange treatment exhibited a slow response speed but also contributed to the synaptic behaviours. **Figure 2** provides a representation of the photosynaptic behaviours of the device. In Figure 2a, the plot illustrates the variation in the current of the heterojunction phototransistor over time when subjected to stimulation from 520 nm light pulses at different frequencies, each possessing a power of 2 μW. It is evident that as the number of light pulses increased, the channel current gradually rose, showcasing facilitation characteristics. Additionally, wider pulse widths, indicating lower corresponding frequencies, resulted in the accumulation of more photogenerated carriers, leading to higher photocurrent levels. Figure 2b portrays the phototransistor's performance under the influence of 520 nm optical pulses at a fixed frequency but varying light power. Higher optical light power corresponds to larger photocurrent. Furthermore, as the number of pulses increased, the photocurrent increments for higher-power optical pulses exceeded that of lower-power pulses. By judiciously controlling the intensity and frequency of optical stimulation, it is possible to achieve an ideal photocurrent difference, thereby modulating pixel contrast in the image. In Figure 2c, the phototransistor 's response to light pulses of varying wavelengths, all possessing the same optical power and pulse frequency, is displayed. Due to the phototransistor's varying absorbance of light at different wavelengths, the photocurrent difference increased as the number of pulses accumulated. For instance, when stimulated by six light pulses, the photocurrent under blue light of 480nm reached 1.5×10^{-7}A, while it registered just 6×10^{-8}A under 520 nm green light irradiation and only 1×10^{-8}A under 630 nm red light irradiation. This pronounced disparity in photocurrents also translated into varying durations for the device to return to its initial dark state current level after light removal. Consequently,

within a defined timeframe, the phototransistor exhibited distinct memory capabilities in response to different wavelengths of light. This behaviour holds significant promise for applications in colour resolution preprocessing of images.

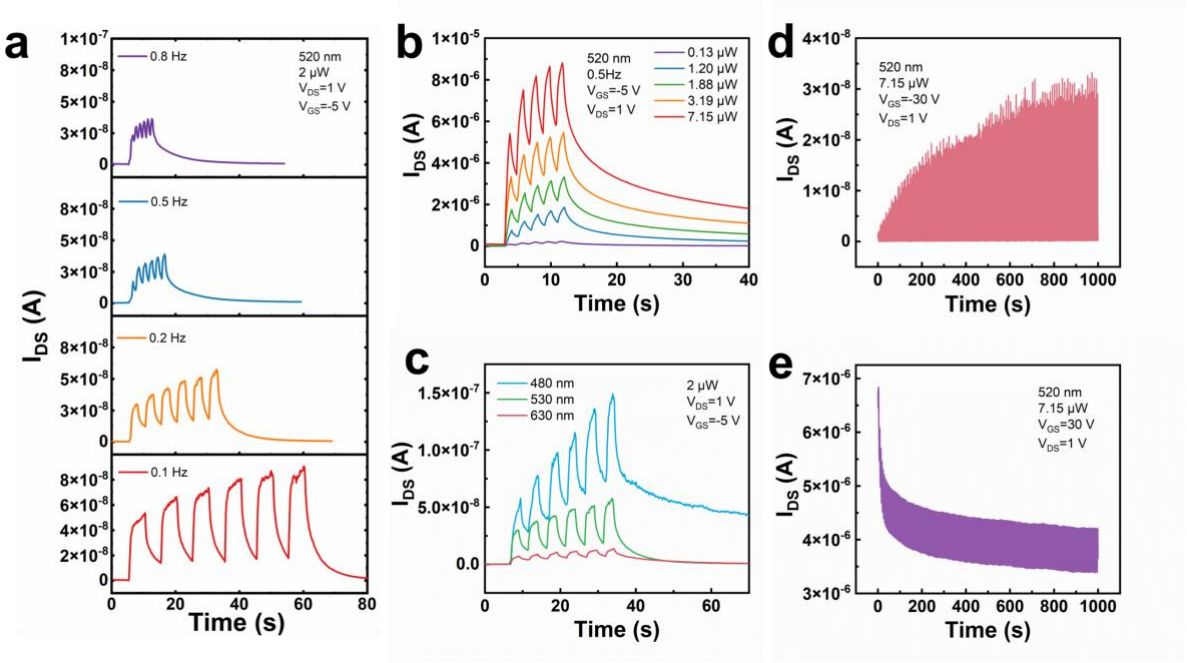

Figure 2. The transient photocurrent response of the phototransistor under the stimulation of (a) green light pulses with different frequencies and fixed power; (b) green light pulses with different power and fixed frequency; (c) different wavelengths with the same power and frequency. Long-term response of the device at V_G of (d) -30 V and (e) 30 V.

Furthermore, the applied gate voltage also had a notable impact on the device's photoresponse behaviours. Figures 2d and 2e illustrate the long-term responses of the device at gate voltages of -20 V and 20 V, respectively. Under continuous negative gate voltage application, the device exhibited a conspicuous current enhancement response when subjected to light pulse stimulation. After 1000 s stimulation of light pulses with pulse frequency of 0.2 Hz and wavelength of 520 nm, the device's photocurrent underwent a significant increase, transitioning from an initial magnitude of 10^{-11} A to a magnitude of 10^{-8} A, indicative of a pronounced enhancement effect. Conversely, when a continuous positive gate voltage was applied, the device displayed current suppression behaviour upon exposure to light pulse stimulation. Following 1000 s stimulation of the same light pulses, the device's photocurrent decreased from an initial 6.8 μA to 4.2 μA. Although the change did not constitute a substantial order of magnitude difference, the reduction in absolute photocurrent value remained clearly discernible. In this context, both the gate voltage and the illumination stimulus jointly influenced the phototransistor's performance. On one hand, continuous optical pulse stimulation

augmented the photocurrent. On the other hand, the gate voltage applied across the device's longitudinal cross-section influenced the internal electric field within the heterojunction formed by CIZS QDs and IGZO. A negative gate voltage heightened the intrinsic built-in potential of the heterojunction, promoting the separation of photogenerated carriers and consequent photocurrent increased—consistent with the impact of light pulses. On the contrary, a positive gate voltage diminished the built-in potential, reducing the efficiency of electron transfer into the IGZO layer and increasing the likelihood of recombination with photogenerated holes trapped within the QDs. Consequently, this reduction in photocurrent occurred. The influence of the positive gate voltage competed with the effect of light pulse stimulation, resulting in a current suppression tendency, particularly noticeable when optical power was low and the positive gate voltage was high.

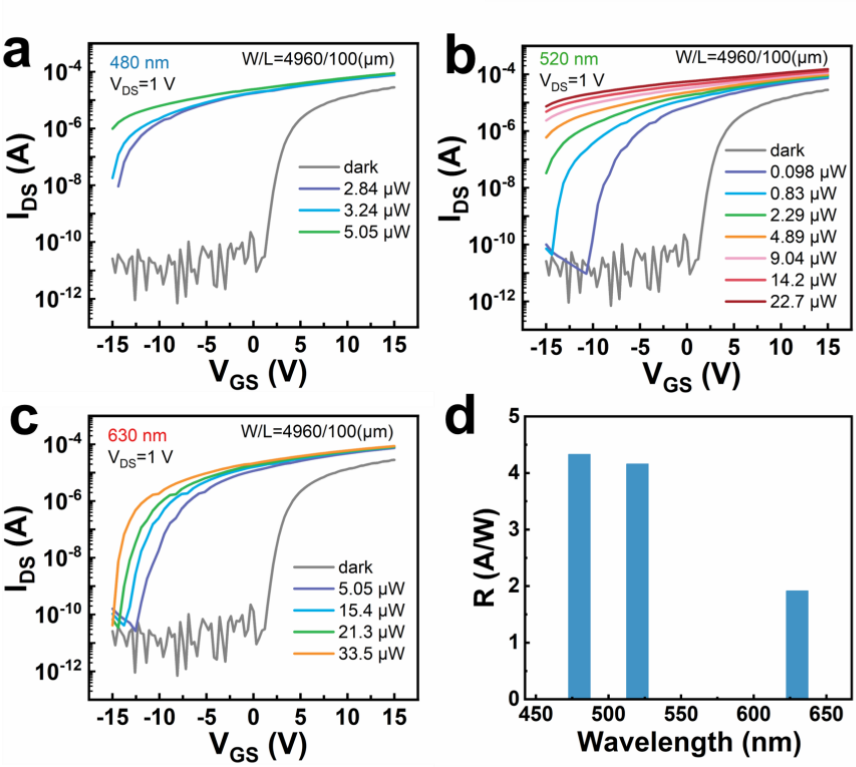

Figure 3. The transfer characteristic curve of the phototransistor with interdigital electrodes at wavelength of (a) 480nm; (b) 520 nm; (c) 630. (d) R and D* at different wavelength.

These tests demonstrated the notable light response capabilities of CIZS QDs/IGZO heterojunction phototransistors across the spectrum spanning from 480 to 630 nm. Furthermore, the adjustment of response speed via surface ligands underscored their potential to cater to distinct application scenarios, aligning with both conventional photoelectric detection and

neuromorphic sensor components. The device's compact size served as a foundational element for constructing high-density photodetector arrays. Additionally, we have also fabricated CIZS QDs/IGZO heterojunction phototransistors with larger size and higher W/L ratios, equipped with interdigital electrodes and an equivalent W/L ratio of approximately 4960/100 μm. An optical microscopic image of this device is presented in Figure S7. The transfer characteristic curves of the device under red, green, and blue light at various power levels are depicted in **Figure 3**a-c, confirming the device's robust light response. For photodetectors, two pivotal parameters are photoresponsivity (R) and specific detectivity (D*). R is generally used to measuring the photodetector's photoelectric conversion efficiency and can be calculated by the equation: $R = \frac{I_{ph}}{P_{in}}$. Here, I_{ph} represents the photogenerated current that is the difference value of device current under light and dark state, P_{in} is incident optical of the photodetector's active area.[30] D* is basically used to evaluate a photodetector's detection capability of weak light. It can be defined as $D* = \frac{R\sqrt{AB}}{i_{niose}}$, where A is device active area an B means the frequency of electrical signal in unit of Hz. i_{niose} is the noise current, which is mainly composed of three parts: shot noise reflected by dark current, thermal Johnson noise, and flicker noise (1/f noise). In many cases, shot noise is regarded as the main part and the D* can be evaluated as $D* = R\sqrt{\frac{A}{2qI_{dark}}}$, q is the elementary charge and I_{dark} is dark current of photodetector.[31] Here, the latter calculation method was taken. These parameters were influenced by the light power and voltage applied to the device. Figure S8a portrays the R and D* values of the device under green light at varying optical power levels. Under 520 nm illumination with a power of 0.1 μW, the heterojunction phototransistor has a R of 60 AW^{-1} and a D* of 2×10^{15} Jones at a gate voltage (V_G) of -0.9 V and drain voltage (V_D) of 1 V. As optical power increased, the number of photogenerated carriers in the device rose. However, due to the larger electrode spacing in the phototransistor structure, carrier recombination occurred, resulting in a corresponding decrease in R and D*. Figure S8b demonstrates the R and D* values at different gate voltages, derived from the data in Figure 3b. Figure S8c provides the optical response of the device at different source-drain voltages, enabling the determination of R and D* under corresponding conditions (Figure S8d). In N-type transistors, higher gate and source-drain voltages yield larger channel currents in the device, consequently leading to heightened responsiveness. However, it is worth noting that the device's dark current is significantly influenced by the gate voltage. As such, the peak detection rate occurs at a gate voltage characterized by low dark current and high light current. In practical applications, the device performance can be adjusted based on specific

requirements. Moreover, due to varying light absorption characteristics across different wavelength bands, the phototransistor generated different photocurrents, resulting in differences in responsiveness. Figure 3d illustrates the comparison of R and D* under three different wavelengths. The device exhibited enhanced absorption properties under blue and green light, resulting in significantly higher R and D* compared to red light.

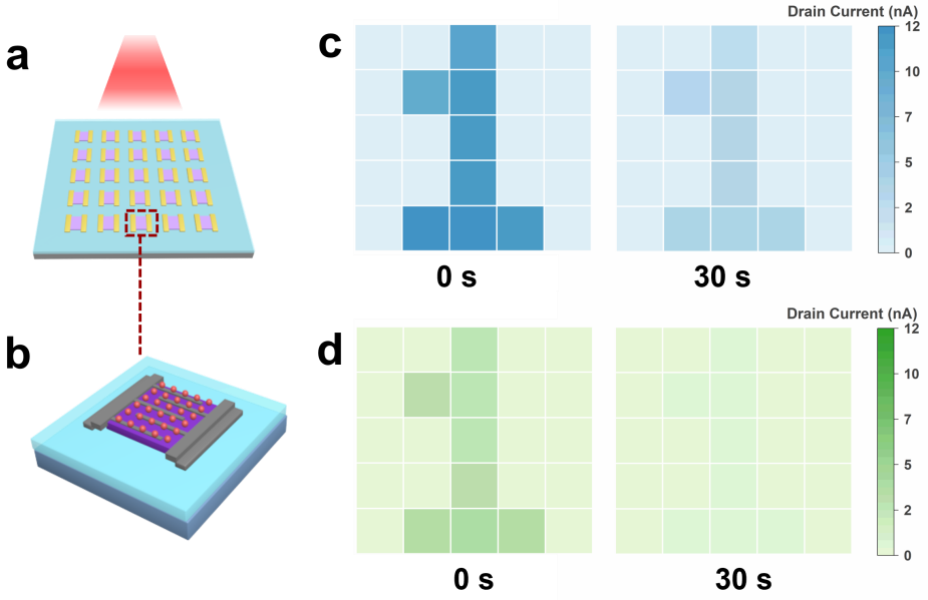

Figure 4. Schematic diagram of (a) a 5×5 phototransistor array and (b) a single device. The image displayed by the array when the (c) blue and (d) green light with power of 2 μW was just off and 30 s later. V_G=-5 V, V_D=1 V.

To illuminate the potential applications of the optical synaptic behaviour exhibited by the device, we assembled a 5×5 array comprising the heterojunction phototransistor with interdigital electrodes. The schematic diagram of this array is depicted in **Figure 4**a, where each individual device (Figure 4b) within the array operated as an optical synapse. The dark current observed in each pixel of the array registered in the order of picoamperes and exhibits commendable uniformity. Firstly, we demonstrated that the array exhibits varying memory effects for different colours of light. We irradiated the pixels of the array with blue light of 480 nm wavelength in the configuration of a digital "1". The illumination was removed once the current reached saturation. Figure 4c displays the images captured by the array immediately after light removal and again 30 s later. Notably, the device's channel current experienced a slight decrease after 30 s, but the image remained relatively distinct. Subsequently, when we irradiated the array with green light of 520 nm at the same power, Figure 4d showcases the images captured by the array right after light removal and once again after a 30 s interval. Due

to the shorter recovery time associated with green light, the image virtually disappeared after 30 s. This discrepancy in current recovery time exhibited by devices for light of different wavelengths holds significant potential for applications in colour recognition.

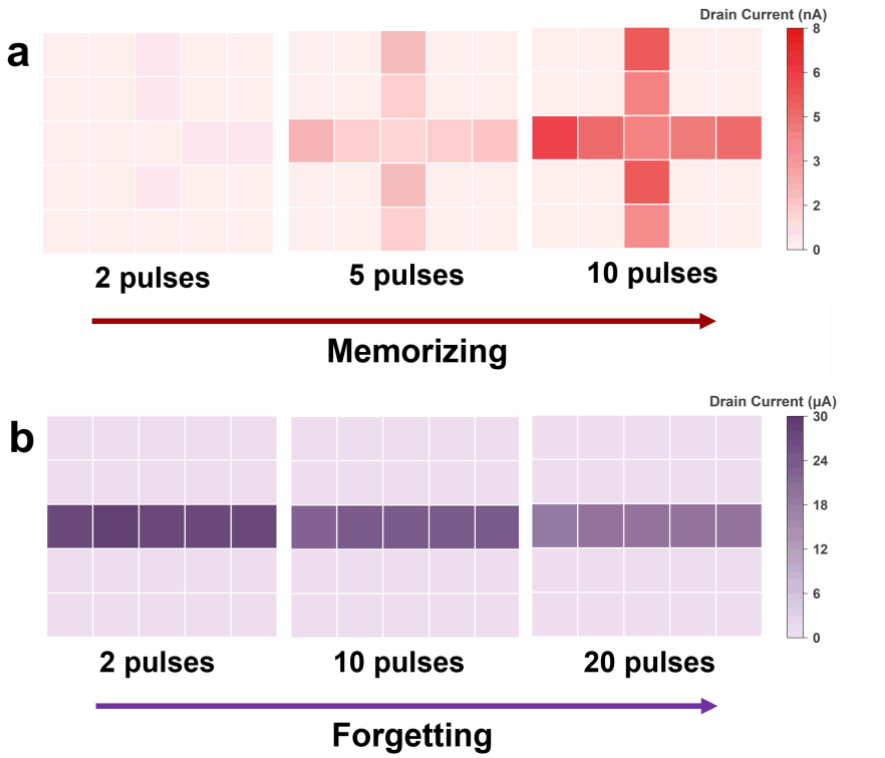

Figure 5. (a) The images stimulated by 2, 5 and 10 green light pulses (2 μW, 0.2 Hz) at negative gate bias (V_G=-20 V, V_D=1 V). (b)The images stimulated by 2, 10 and 20 green light pulses (2 μW, 0.2 Hz) at positive gate bias (V_G=20 V, V_D=1 V).

Subsequently, we applied a gate voltage of -20V to the device array and successively introduced 520nm green light pulses to the pixels of the array, shaping them into a plus sign. The images resulting from stimulation with 2, 5, and 10 pulses exhibited distinct enhancement effects, as depicted in **Figure 5**a. Conversely, we applied a gate voltage of +20V and introduced 520nm green light pulses to the pixels of the array in the configuration of a minus sign. The images resulting from stimulation with 2, 10, and 20 pulses exhibited a certain inhibitory effect, as shown in Figure 5b. The enhancement and suppression of current under varying gate voltages can be utilized to simulate memory and forgetting behaviours akin to those observed in the optic nerve. These synaptic behaviours simulations validated the potential applications of the heterojunction phototransistor device in image information preprocessing and it is satisfying that based on the existing experimental data, the device's performance displays relative

uniformity. Besides, a few reported colloidal QDs/mental oxide phototransistors are compared in **Table 1**, [7,8,20] which reflected that the device in this work takes advantages in multifunction and environmental safety while keep the high detectivity. However, it's important to note that the current device fabrication process imposes limitations on the array size. Therefore, in future research endeavours, we intend to reduce the device size and increase the number of pixels, a development that promises to further enhance the utility of the heterojunction phototransistor device in the field of neuromorphic vision sensing.

Table 1. Comparison of colloidal QDs/mental oxide heterojunction phototransistors.

Device	**Response range (nm)**	**D* (Jones)**	**Working mode (Synaptic mode /Imaging mode)**	**Environmental safety**	**Ref.**
CdS-CdSe QDs/IGZO	405-635	2.5×10^{15}	Synaptic mode	No	[8]
CdSe QDs/IGZO	400-635	3.5×10^{15}	Synaptic mode	No	[20]
InP-ZnSe QDs/SnO_2	520	-	Synaptic mode	Yes	[7]
CIZS QDs/IGZO	480-630	3.4×10^{15}	Both	Yes	This work

3. Conclusion

In summary, we have successfully fabricated CIZS QDs/IGZO heterojunction phototransistor with excellent photoresponse to visible light. By utilizing different ligands, we can adjust the optical response speed of the device, thereby tailoring it for various application scenarios. Short-chain ligand QD devices demonstrate rapid response speeds, making them well-suited for typical image sensing applications. On the other hand, long-chain ligand QD devices exhibit optical synaptic behaviours, which are intricately linked to factors such as the intensity, frequency and wavelength of light pulse stimulation, and also applied gate voltage. These devices can perform functions such as colour recognition, visual memory, and forgetting, among others. This versatility positions the device for potential applications in image preprocessing, offering valuable insights for the development of next-generation bionic vision imaging systems.

4. Experimental Methods

Materials: Copper iodide (CuI, 99.998%), indium acetate (In(OAc)3, 99.99%), diphenyl diselenide (for synthesis grade), oleylamine (Oam, 95%), 1-octadecene (ODE, 90%), and diphenylphosphine (DPP, 98%), Sulfur powder (98%) and zinc acetate (Zn(Oac)2, 99.99%) were obtained from Sigma-Aldrich. All chemicals were used as received without further treatment.

Synthesis of QDs: The CIZS QDs were made using a modified method detailed in a previously published work.[23,32,33] To prepare the sulfur precursor (1.0 M), we dissolved sulfur powder in diphenyl ether (DPP), while the selenium precursor (1.0 M) was made by dissolving diphenyl diselenide in a DPP mixture. For the synthesis of the CIZSSe QDs, we combined In(Oac)3 (0.2 mmol), CuI (0.14 mmol), Zn(Oac)2 (0.08 mmol), Oleylamine (ODE) (3.0 mL), and Octadecene (Oam) (4.0 mL) in a flask. The solution was then degassed under vacuum at 100°C for 5 minutes before being heated to 180°C in a nitrogen (N2) environment. Subsequently, a 1:1 mixture of selenium and sulfur (0.25 mL of selenium precursor and 0.5 mL of sulfur precursor) was rapidly injected, and the reaction was allowed to proceed for 3 minutes. The system was then further heated to 220°C and maintained for an additional 8 minutes. Finally, the obtained QDs were purified through centrifugation with the addition of ethanol.

Device Fabrication: We began with a heavily doped N-type silicon wafer featuring a 180nm oxide layer as our device substrate. After a thorough cleaning process involving acetone, ethanol, and deionized water, we deposited a 35nm-thick IGZO film onto the substrate using a magnetron sputtering process. This film was then annealed at 300°C in an oxygen-rich environment for one and a half hours in a tube furnace. For the device's source and drain electrodes (Mo), we utilized a magnetron sputtering process, resulting in an approximately 80nm thickness. The patterns of the active layer and source-drain electrodes were defined using standard photolithography, followed by wet etching or stripping processes. The CZIS QDs was diluted to a concentration of about 20mg/ml, and was filtered before use. Then the QDs layer was spin-coated onto the transistor's surface at speed of 1000 turns per minute to achieve a 100nm thickness. The assembly is subsequently placed on a 100℃-heating table for 10 minutes to facilitate solvent evaporation.

Surface Ligand Treatment: In this process, EDT (4‰ in acetonitrile) was applied to the surface of the quantum dot device for 30 s. Subsequently, EDT was removed through rotation. Then excess EDT molecules were eliminated by a rinse-spin step with acetonitrile immediately.

Device Characteristics: Electrical measurements of the IGZO TFT were conducted at room temperature within a probe station (Cascade MPS150) and were connected to a sourcemeter (Keysight Agilent B1500A). For the optoelectrical evaluations of the CZIS QDs/IGZO phototransistor, a Keithley 6482 sourcemeter was employed. Monochromatic green light at 520

nm was generated using a laser (Nanjing Metatest Corp.), while blue light at 480 nm and red light at 630 nm were provided by light sourced and wavelength selection equipment (SC-5 and AOTF, Wuhan Yangtze Soton Laser Co., Ltd.). Light pulses at specific frequencies were generated using a laser controller (Rigol DG822). To regulate incident light power levels, the light systems were equipped with optical attenuators. An optical power meter (ThorLabs PM100A meter and S120VC searching unit) was utilized to calibrate the light power.

Material Characteristics: The morphology of the CIZS QDs film and the cross-section structure of the phototransistor were examined using SEM (Carl Zeiss Supra 55). HRTEM (Tecnai G2 300 kV) was employed to observe the QDs at a high resolution. The UV-vis absorption spectrum of the QDs was recorded using a spectrophotometer (Shimadzu UV-2600). To analyze the energy levels of the QDs, UPS (Thermo Fisher ESCALAB 250Xi) was employed.

Supporting Information

Supporting Information is available from the Wiley Online Library or from the author.

Acknowledgements

This work is supported by Shenzhen Municipal Scientific Program under Grants (JCYJ2020010914061043), National Natural Science Foundation of China (61904006), EPSRC SWIMS (EP/V039717/1) and Royal Society (RGS\R1\221009 and IEC\NSFC\211201).

Received: ((will be filled in by the editorial staff))
Revised: ((will be filled in by the editorial staff))
Published online: ((will be filled in by the editorial staff))

References

[1] S. W. Cho, C. Jo, Y.-H. Kim, S.-K. Park, *Nano-Micro Lett.* **2022**, *203*, 1.
[2] Y. Chai, *JMS* **2020**, *23*, 54.
[3] F. Liao, Z. Zhou, B. J. Kim, J. Chen, J. Wang, T. Wan, Y. Zhou, A. T. Hoang, C. Wang, J. Kang, J.-H. Ahn, Y. Chai, *Nat Electron* **2022**, *5*, 84.
[4] F. Zhou, Z. Zhou, J. Chen, T. H. Choy, J. Wang, N. Zhang, Z. Lin, S. Yu, J. Kang, H.-S. P. Wong, Y. Chai, *Nat. Nanotechnol.* **2019**, *14*, 776.
[5] S. Hong, H. Cho, B. H. Kang, K. Park, D. Akinwande, H. J. Kim, S. Kim, *ACS Nano* **2021**, *15*, 15362.

[6] T. Jiang, Y. Wang, Y. Zheng, L. Wang, X. He, L. Li, Y. Deng, H. Dong, H. Tian, Y. Geng, L. Xie, Y. Lei, H. Ling, D. Ji, W. Hu, *Nat Commun* **2023**, *14*, 2281.

[7] K. Liang, R. Wang, B. Huo, H. Ren, D. Li, Y. Wang, Y. Tang, Y. Chen, C. Song, F. Li, B. Ji, H. Wang, B. Zhu, *ACS Nano* **2022**, *16*, 8651.

[8] C. Jo, J. Kim, J. Y. Kwak, S. M. Kwon, J. B. Park, J. Kim, G. Park, M. Kim, Y. Kim, S. K. Park, *Adv. Mater.* **2022**, *34*, 2108979.

[9] N. Jiang, J. Tang, W. Zhang, Y. Li, N. Li, X. Li, X. Chen, R. Fang, Z. Guo, F. Wang, J. Wang, Z. Li, C. He, G. Zhang, Z. Wang, D. Shang, *Adv. Optical Mater.* **2023**, 2300271.

[10] Y. Sun, Y. Ding, D. Xie, J. Xu, M. Sun, P. Yang, Y. Zhang, *Adv. Optical Mater.* **2021**, *9*, DOI: 10.1002/adom.202002232.

[11] K. Liang, R. Wang, H. Ren, D. Li, Y. Tang, Y. Wang, Y. Chen, C. Song, F. Li, G. Liu, H. Wang, W. R. Leow, B. Zhu, *Adv. Optical Mater.* **2022**, *10*, 2201754.

[12] T. Kamiya, K. Nomura, H. Hosono, *J. Display Technol.* **2009**, *5*, 273.

[13] Y. Zhu, Y. He, S. Jiang, L. Zhu, C. Chen, Q. Wan, *J. Semicond.* **2021**, *42*, 031101.

[14] T. Kamiya, H. Hosono, *NPG Asia Mater* **2010**, *2*, 15.

[15] T. Chen, C. Wang, G. Yang, Q. Lou, Q. Lin, S. Zhang, H. Zhou, *Adv Materials Technologies* **2022**, *8*, 2200679.

[16] B. H. Kang, K. Park, M. Hambsch, S. Hong, H. T. Kim, D. H. Choi, J. H. Lee, S. Kim, H. J. Kim, *Nano Energy* **2022**, *92*, 106773.

[17] H. Ferhati, F. Djeffal, L. B. Drissi, *Superlattices. Microstruct.* **2021**, *156*, 106967.

[18] J. Kim, C. Jo, M. Kim, G. Park, T. J. Marks, A. Facchetti, S. K. Park, *Adv. Mater.* **2021**, *34*, 2106215.

[19] Z. Xin, Y. Tan, T. Chen, E. Iranmanesh, L. Li, K.-C. Chang, S. Zhang, C. Liu, H. Zhou, *Nanoscale Adv.* **2021**, *3*, 5046.

[20] E. Fu, Y. Liu, X.-R. Hou, Y. Feng, C. Yang, Y. Shao, *Nanoscale Res Lett* **2022**, *17*, 102.

[21] H. Duan, L. Liang, Z. Wu, H. Zhang, L. Huang, H. Cao, *ACS Appl. Mater. Interfaces* **2021**, *13*, 30165.

[22] M. Kimura, T. Kamiya, T. Matsuda, K. Umeda, A. Fukawa, Y. Nakashima, *SID Symp. Dig. Tech. Pap.* **2018**, *49*, 512.

[23] B. Hou, M. Sohn, Y.-W. Lee, J. Zhang, J. I. Sohn, H. Kim, S. Cha, J. M. Kim, *Nano Energy* **2019**, *62*, 764.

[24] B. Hou, D. Benito-Alifonso, N. Kattan, D. Cherns, M. C. Galan, D. J. Fermín, *Chem. Eur. J.* **2013**, *19*, 15847.

[25] S. W. Seo, J.-O. Jeon, J. W. Seo, Y. Y. Yu, J. Jeong, D.-K. Lee, H. Kim, M. J. Ko, H. J. Son, H. W. Jang, J. Y. Kim, *ChemSusChem* **2016**, *9*, 439.

[26] Y. Liu, K. Jiang, Y. Nie, Y. Guo, Q. Ma, *Anal Bioanal Chem* **2020**, *412*, 1893.

[27] F. Xu, X. Ma, C. R. Haughn, J. Benavides, M. F. Doty, S. G. Cloutier, *ACS Nano* **2011**, *5*, 9950.

[28] Z. L. Teh, L. Hu, Z. Zhang, A. R. Gentle, Z. Chen, Y. Gao, L. Yuan, Y. Hu, T. Wu, R. J. Patterson, S. Huang, *ACS Appl. Mater. Interfaces* **2020**, *12*, 22751.

[29] M. Yang, H. Liu, S. Wen, Y. Du, F. Gao, *Materials* **2022**, *15*, 9058.

[30] R. Saran, R. J. Curry, *Nature Photon* **2016**, *10*, 81.

[31] F. P. García de Arquer, A. Armin, P. Meredith, E. H. Sargent, *Nat Rev Mater* **2017**, *2*, 16100.

[32] S.-B. Cho, J. I. Sohn, S.-S. Lee, S.-G. Moon, B. Hou, I.-K. Park, *J. Mater. Chem. C* **2021**, *9*, 7027.

[33] H. Song, Y. Lin, Z. Zhang, H. Rao, W. Wang, Y. Fang, Z. Pan, X. Zhong, *J. Am. Chem. Soc.* **2021**, *143*, 4790.

The table of contents entry should be 50–60 words long and should be written in the present tense. The text should be different from the abstract text.

A Low-Toxic Colloidal Quantum Dots Sensitized IGZO Phototransistor Array for Neuromorphic Vision Sensors

Tong Chen[1], Shijie Zhan[2], Benxuan Li[2,3], Bo Hou[2], Hang Zhou[1]**

ToC figure ((Please choose one size: 55 mm broad × 50 mm high **or** 110 mm broad × 20 mm high. Please do not use any other dimensions))

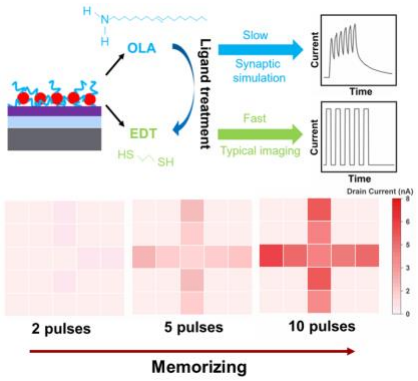

A heterojunction phototransistor based on IGZO and low-toxic colloidal quantum dots was developed and the response speed could be tuned via quantum dot ligand treatment. Short-chain ligands enable typical sensing, while long-chain ligands emulate photosynaptic functions such as color recognition, visual memory, and forgetting. This novel device has potential in optoelectronics and neuromorphic visual memory applications.

Supporting Information

A Low-Toxic Colloidal Quantum Dots Sensitized IGZO Phototransistor Array for Neuromorphic Vision Sensors

Tong Chen[1], Shijie Zhan[2], Benxuan Li[2,3], Bo Hou[2], Hang Zhou[1]**

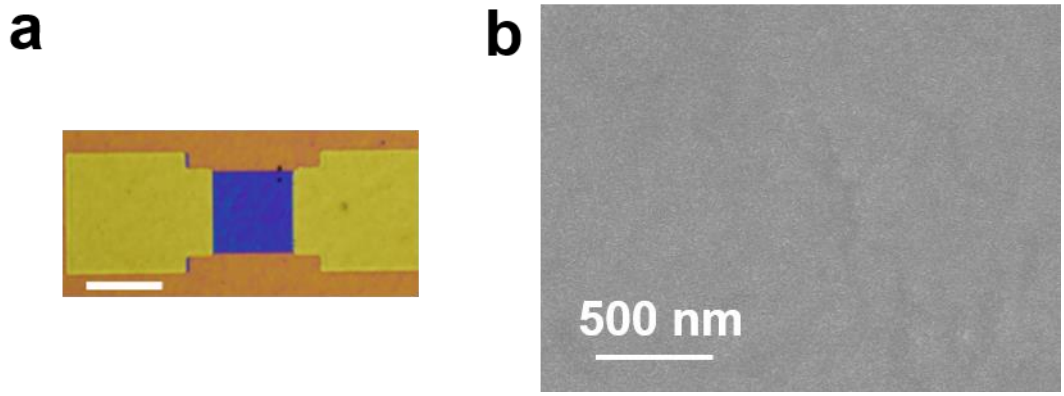

Figure S1. (a) Optical microscope images of CIZS QDs/IGZO phototransistor with W/L of 100 μm/100 μm, scale bar is 100 μm. (b) SEM image of the CIZS QDs film.

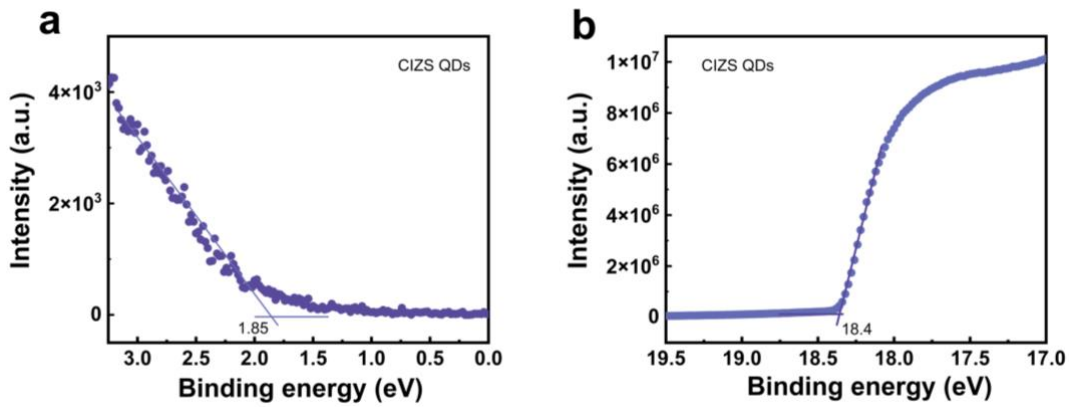

Figure S2. (a) Low and (b) high energy regions in UPS of the CIZS QDs.

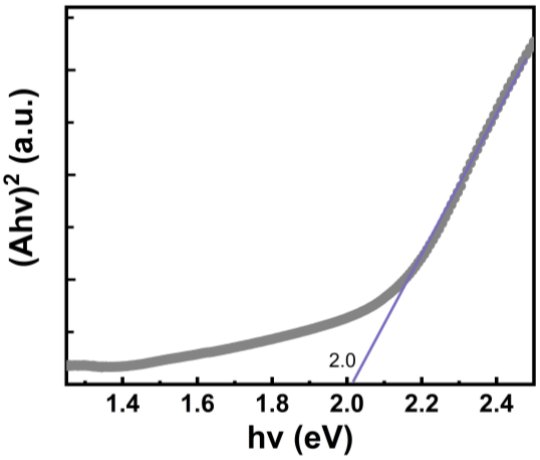

Figure S3. Tauc plots of the CIZS QDs.

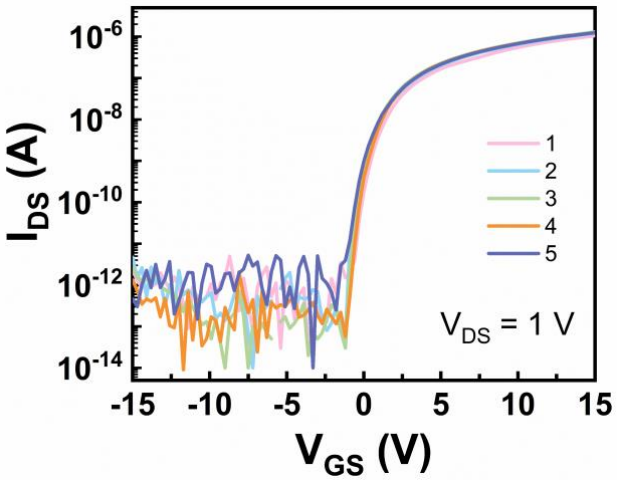

Figure S4. Transfer characteristic curves of 5 different IGZO TFTs with W/L of 100 μm/100 μm.

Table S1. The average values of key performance parameters for the IGZO TFTs in Figure S4.

Parameters (units)	Mean values
I_{off} (A)	2.51×10^{-13}
I_{on}/I_{off}	1.92×10^{7}
μ ($cm^2V^{-1}s^{-1}$)	6.02
SS ($Vdec^{-1}$)	0.21

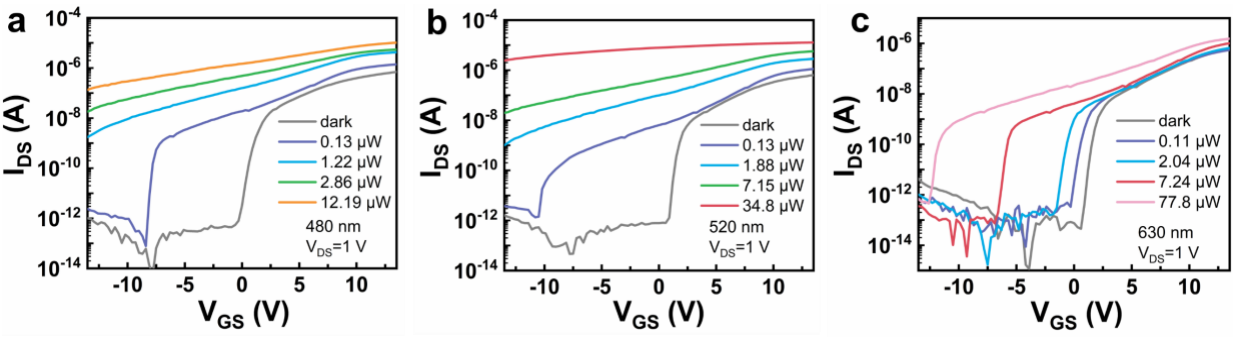

Figure S5. Optical response of the small-size (W/L=100 μm/100 μm) device under light of (a) 480 nm; (b) 520 nm; (c) 630 nm.

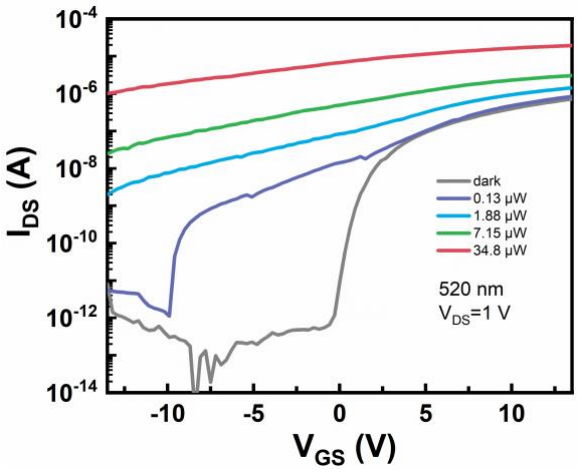

Figure S6. Optical response of the small-size device that was treated with surface ligand EDT under light of 520 nm.

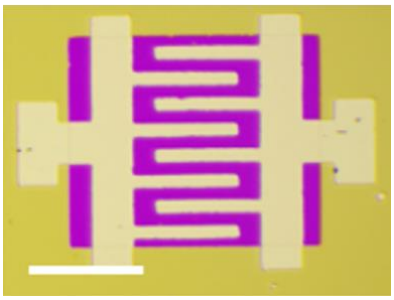

Figure S7. Optical microscope images of CIZS QDs/IGZO phototransistor with interdigital electrodes with W/L of 4960 μm/100 μm, scale bar is 500 μm.

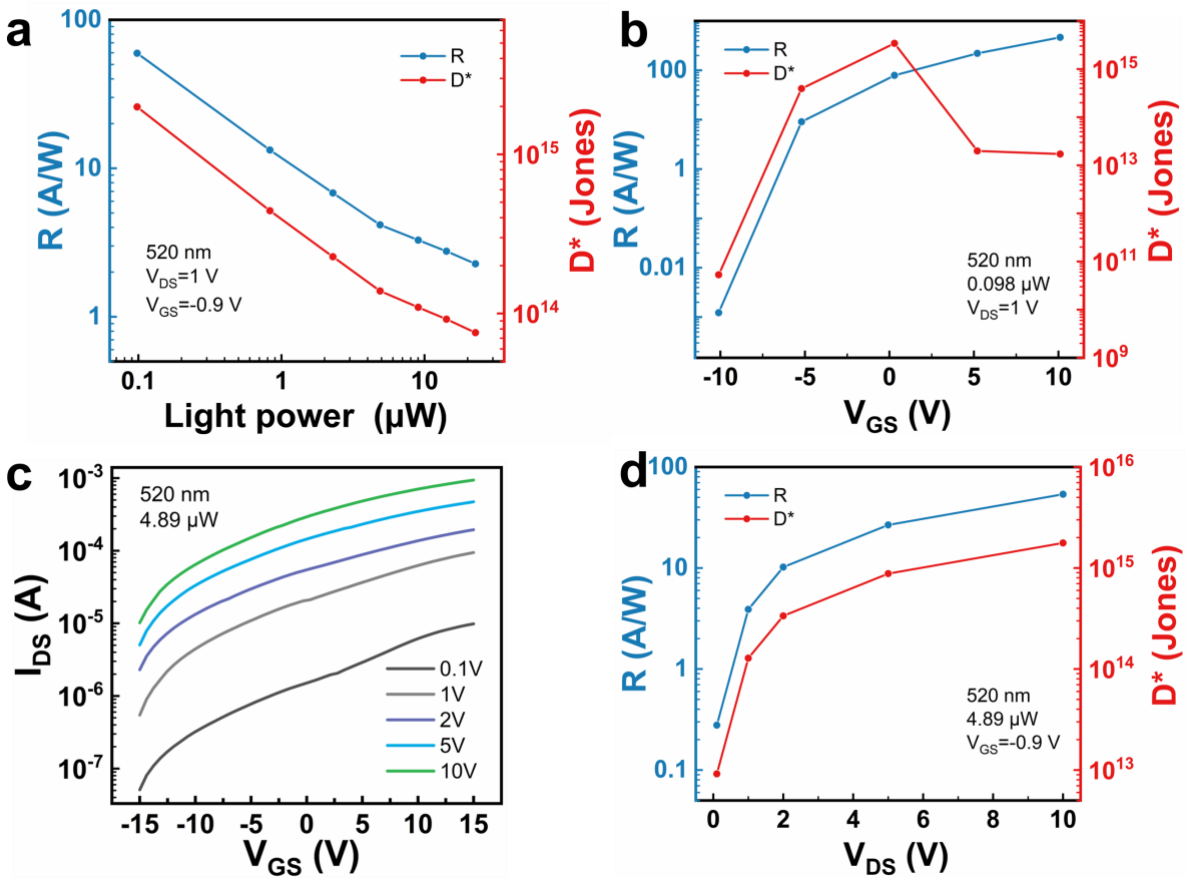

Figure S8. R and D at different (a) light power and (b) V_G of the big-size (W/L=4960 μm /100 μm) phototransistor under green light derived from Figure 4b. (c) The transfer characteristic curve of the big-size phototransistor under green light at various V_D. (d) R and D at various V_D.